

## **A 3D THERMAL-POROELASTIC MODEL FOR GEOTHERMAL RESERVOIR STIMULATION**

Xiaonan Wang and Ahmad Ghassemi

Texas A&M University  
Department of Petroleum Engineering  
College Station, TX, 77843, U.S.  
e-mail: [ahmad.ghassemi@pe.tamu.edu](mailto:ahmad.ghassemi@pe.tamu.edu)

### **ABSTRACT**

One of the most important tasks for geothermal reservoir development is engineering a fractured reservoir and predicting its future performance. For this purpose, numerical modeling of fluid flow and deformation of fractured rock is necessary. This work focuses on utilizing a stochastic fracture network and poroelasticity to simulate the thermal-hydro-mechanical response of the reservoir during the stimulation process, and to assess the permeability enhancement in the stimulated zone. The reservoir stimulation process is simulated using a system of rock blocks some of which contain stochastically-distributed fractures and fractured zones. The effect of the fractures on permeability is introduced into the model by using the equivalent permeability approach. The rock matrix is assumed to be poroelastic and the fractures are allowed to deform and to slip. Heat transport within the fractures and the associated thermal stress on the fractures is also considered. A series of simulations are carried out to analyze the rock mechanical response and permeability evolution for a Newberry-type reservoir. Results show the significant role of fracture distribution and its mechanical deformation in EGS design and development. This model provides a tool to predict the performance of natural fracture networks, and to analyze the stimulation response and future production performance.

### **INTRODUCTION**

Simulation of the response of an engineered geothermal reservoir generally requires analyzing the thermo-poroelastic response of the reservoir rock as well as the natural fracture opening and propagation. These three parts are not independent from each other during the stimulation process and tend to strongly affect each other.

There are generally two classes of fracture models, stochastic fracture network models (Cladhuous et al. 2011; Bruel et al. 1994; Willis-Richards et al. 1996; and Tezuka et al. 2005) and deterministic models (Kolditz and Clauser 1998, Ghassemi et al. 2007, and Safari and Ghassemi 2011). There are also works that utilize combined deterministic and stochastic fracture networks (e.g., Tezuka and Watanabe 2000). In these works on reservoir stimulation and fracture modeling, the thermo-poroelastic coupling process has been either neglected or simplified to empirical correlations (Cladhuous et al. 2011; Bruel, 2002; Willis-Richards et al. 1996). Three-dimensional coupled thermo-poro-mechanical models have been developed and applied to reservoir stimulation, development, and well bore stability analysis (Zhou and Ghassemi, 2009; Lee and Ghassemi, 2011). However, the reservoir rock was modeled as continuous porous media with possibly a few major fractures.

In this work, a fracture network is introduced into a coupled poroelastic model with heat transport. Poroelastic stresses in the rock matrix are computed at each time step, and are interpolated onto the natural fracture faces when calculating the fracture aperture change. The rock mass permeability is estimated using the equivalent permeability (Tezuka and Watanabe 2000). An iterative method is employed to retrieve the stress dependent permeability at each time step. Considering the complexity of the problem and the computational cost, the rock strain and fracture geometry change are considered independent from the thermal response at this stage. The heat transport in the rock mass is assumed to occur via fluid flow within the fractures, and the heat conduction from rock matrix to the fracture flow is assumed to be linear.

Simulation examples are performed in this paper to illustrate the various aspects of reservoir stimulation

and model predictions. In the near wellbore test case, a small-scale simulation domain is used and the permeability development, as well as pore pressure diffusion is computed. In the reservoir response test case, the stress distribution and fracture slip are studied and the potential sites of micro-seismic events are recorded. Finally, an example of heat transfer calculation is presented. The results show that the current model is capable of simulating cold water injection test for EGS.

## **STOCHASTIC FRACTURE NETWORKS**

In this work, the reservoir consists of block of rock containing a stochastic fracture network. The 3D hydraulically conductive fracture network is generated using stochastic descriptions of its characteristics (Cacas et al. 1990): Poisson distribution (fracture location), log-normal distribution (fracture size), and Fisher von Mises distribution (fracture orientation). The parameters of these distributions are usually found from field tests or experimental tests. The fracture data can be compiled in to a network by defining their location, size, and orientation. One sample of such stochastic fracture network (Table 1) is shown in Fig. 1. The parameters of the fracture distribution are from fracture analysis of Newbery filed (NWG 55-29, ALTAROCK ENERGY INC., 2011), and from empirical suggestions (Cacas et al. 1990). Fracture apertures are assigned following the relationship with the fracture size (Tezuka and Watanabe 2000):

$$a = \alpha\sqrt{r} \quad (1)$$

Table 1: Parameters of the probability functions of stochastic fractures

Density [m <sup>-1</sup> ]	1.0
Mean of the log(radius) [radius in meters]	0
Standard deviation of the log(radius) [radius in meters]	0.7
Fisher von Mises distribution parameter	2.8
$\alpha$	4.0 × 10 <sup>-3</sup>
Number of fractures	500

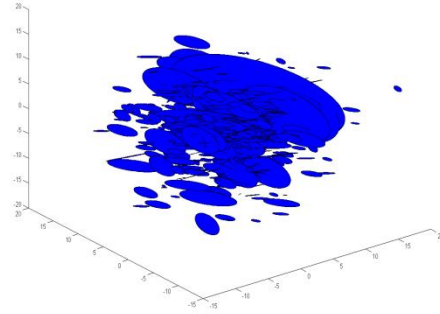


Figure 1: A stochastic fracture network.

## **POROELASTIC MODEL EQUATIONS**

The general constitutive equations for the poroelastic model can be written as (compression positive; incremental formula):

$$\dot{\sigma}_{ij} = 2G\dot{\varepsilon}_{ij} + \left(K - \frac{2G}{3}\right)\dot{\varepsilon}_{kk}\delta_{ij} + \alpha\dot{p}\delta_{ij} \quad (2)$$

$$\dot{\zeta} = \alpha\dot{\varepsilon}_{ij} + \beta\dot{p} \quad (3)$$

$$\beta = \frac{\alpha - \phi}{K_s} + \frac{\phi}{K_f} \quad (4)$$

Where  $\sigma_{ij}$  and  $\varepsilon_{ij}$  are the total stress and strain components.  $p$  is the pore pressure components.  $\alpha$  is the Biot's coefficient.  $\phi$  is the porosity.  $K_s$  and  $K_f$  are the bulk modulus of solid and fluid.  $\zeta$  is the variation of fluid volume per unit reference pore volume.

The finite element formula of the above governing field equations can be derived using a finite element discretization in the 3D domain (Galerkin method) and Crank-Nicolson approximation in time domain (Lee and Ghassemi 2011).

$$\begin{bmatrix} K & A \\ A^T & -(S + \theta\Delta t H_H) \end{bmatrix} \begin{bmatrix} \Delta \tilde{u} \\ \Delta \tilde{p} \end{bmatrix} = \begin{bmatrix} \Delta f \\ \Delta t H_H \tilde{p}_{t_{n-1}} + \Delta Q \end{bmatrix} \quad (5)$$

$\tilde{u}$  and  $\tilde{p}$  are the vectors of the nodal displacements and nodal pore pressures.  $\theta$  is the Crank-Nicolson approximation parameter, which is set to be 1 in this work.  $\Delta t$  is the time step.  $\Delta f$  is the applied external

force on nodes.  $\Delta Q$  is the source/sink term.  $\tilde{p}_{t_{n-1}}$  is the nodal pore pressure component from previous time step. Other matrices are presented as following.

$$\begin{aligned}
K &= \int_{V_e} B^T D B dV, A = \int_{V_e} B^T \alpha m N_p dV, \\
S &= \int_{V_e} N_p^T \beta N_p dV, \\
H_H &= \int_{V_e} (\nabla N_p)^T (k / \mu) (\nabla N_p) dV
\end{aligned} \tag{6}$$

Where  $[D]$  is the material elastic matrix.  $[B]$  is the strain-displacement matrix.  $m = [1,1,1,0,0,0]^T$ . Also,  $[N_p]$  is the shape function for pore pressure.  $k$  is the element permeability variable, and  $\mu$  is the fluid viscosity.

The above finite element formula is solved for the primary variables  $u$  and  $p$ . Then, the strain variables can be calculated as:

$$[\varepsilon] = [D][B][\hat{u}]$$

The effective stresses at Gauss integral points are calculated using:

$$\dot{\sigma}_{ij}' = 2G \dot{\varepsilon}_{ij} + \left(K - \frac{2G}{3}\right) \dot{\varepsilon}_{kk} \delta_{ij} \tag{7}$$

The updated effective stresses are then interpolated onto the fracture faces when calculating the fracture response (described below).

### **PERMEABILITY OF NATURAL FRACTURED RESERVOIR**

In numerical simulations, the reservoir block is divided into small elements as shown in Fig. 2. The fractures have apertures ( $a$ ) and intersect the elements with an intersection length ( $l$ ). The directional conductivity of the blocks can be expressed in the following way (e.g., Rahman et al. 2002):

$$k_i = \sum_{j=1}^{n_{fi}} \frac{a_j^3 l_{ij}}{12A}, i = x, y, z \tag{8}$$

Where,  $n_{fi}$  is the total number of fractures in the element, which contributes to the flow in  $i^{th}$  directional.  $a_j$  and  $l_{ij}$  are the aperture and intersection line length of the  $j^{th}$  fracture on the intersected element surface.  $d$  is the flow travel length in the corresponding direction, which is the distance between the center of two elements in this model. The total permeability of the individual elements is obtained by the superposition of the rock mass permeability and the equivalent permeability of fractures.

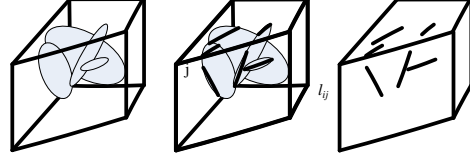


Figure 2: Conversion of fracture permeability into equivalent permeability.

### **Connectivity of fracture networks**

The equivalent permeability technique converts fracture networks into a continuous media with equivalent permeability. The conductivity of the resulting continuous media is dramatically influenced by the connectivity of the fracture network, and is also affected by the finite element mesh selection. The connectivity of the fracture networks used in the stimulation test cases was analyzed, and the results are shown in Fig. 3-4. 500 fractures are created within the domain matrix block. Different fracture orientation distribution parameters are tested. Three sizes of finite element mesh are used.

Fig. 3 shows the influence of fracture orientations on fracture network conductivity. The blue color shows the connectivity of fracture networks whose orientations are derived based on Fisher von Mises distribution (group a) and those with a random distribution (group b). We can see that the fracture network with random orientations has higher conductivity in x- and y-directions and a lower conductivity in the z- direction when compared with Fisher von Mises distributed fracture networks. Considering the geometric average conductivity, group (b) fractures also shows higher values than group (a). These two groups of fractures have the same number of fractures, same fracture size distributions. The finite element meshes are the same as well. From the comparison, we can see the connectivity of fracture networks is significantly influenced by the fracture orientations.

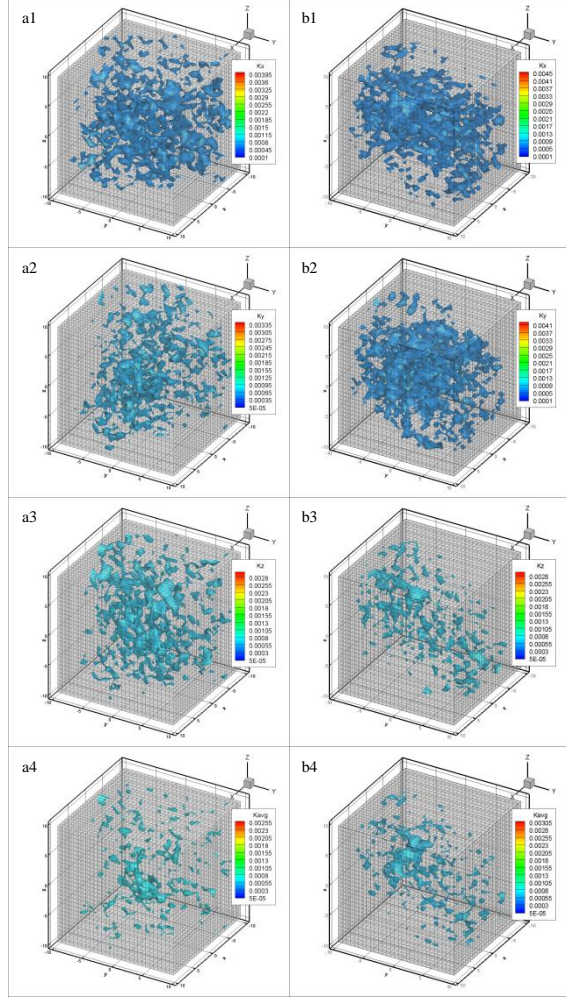


Figure 3: Connectivity of fractures as influenced by fracture orientations.

The equivalent permeability is evaluated on each element's surfaces. Fig. 4 shows the effect of mesh size on the permeability evaluation. The same two group of fractures as above are used. The matrix block is discretized in to 1000, 8000, and 27000 elements respectively for three test cases (a, b, c series in Fig. 4). We can see that after the fractures and the matrix elements are converted to a continuous media, the patterns of heterogeneity of the element conductivity are similar in three cases (a1, b1, c1) with different mesh sizes. However, as can be seen, the finer the mesh the worse the connectivity. For the mesh with 27000 elements, most of the high conductivity zones are isolated. The isolated high conductivity zones will negatively impact fluid flow and heat transfer in the model. Comparing the left side of Fig. 4 (Fisher von Mises distribution) and the figures on right side (random distribution), we can see that the randomly distributed cases have a higher connectivity for all three mesh sizes.

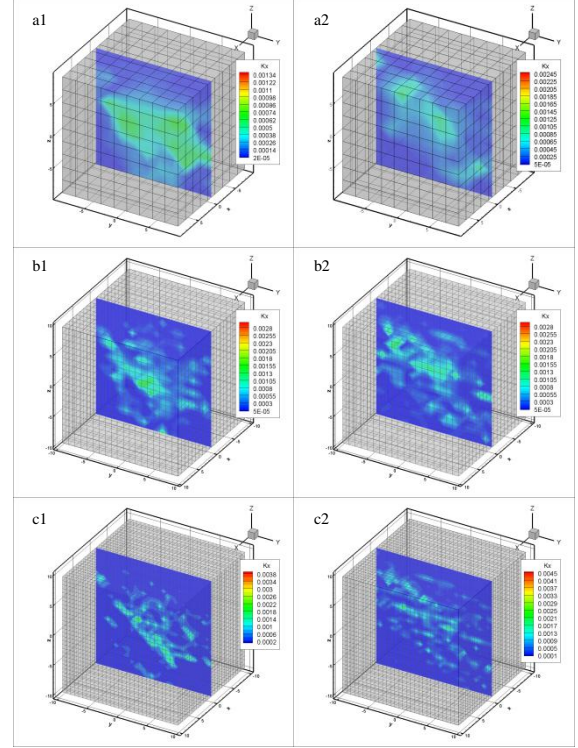


Figure 4: Equivalent element conductivity affected by mesh size.

### Fracture dilation by shear slippage

When the fracture surfaces are in contact, the “in contact” fracture aperture is given by (Willis-Richards et al. 1996):

$$a = \frac{a_0}{1 + 9\sigma_{eff}/\sigma_{nref}} + a_s + a_{res} \quad (9)$$

Where  $a_0$  is the initial fracture aperture;  $a_s$  the change in aperture due to shear dilation;  $a_{res}$  is the residual aperture when effective stress is zero ( $\sigma_{eff} = 0$ ).  $\sigma_{nref}$  is the effective normal stress applied to cause a 90% reduction in the compliant aperture (Willis-Richards et al. 1996). The fracture aperture changes upon deformation and slip. The shear slippage is assumed to be governed by the linear Mohr-Coulomb failure criterion i.e., the shear slippage occurs when the shear stress exceeds the shear strength:

$$\tau_n \geq \sigma_{eff} \tan \varphi; \varphi = \varphi_{basic} + \varphi_{dil}^{eff} \quad (10)$$

Where  $\varphi_{basic}$  is the basic friction angle which can be measured from e.g., laboratory tests. The effective shear dilation angle  $\varphi_{dil}$  can be written in terms of measured shear dilation angle  $\varphi_{dil}$  (Willis-Richards et al. 1996):

$$\varphi_{dil}^{eff} = \frac{\varphi_{dil}}{1 + 9\sigma_{eff}/\sigma_{nref}} \quad (11)$$

Shear slippage will result in a shear displacement which can significantly affect the permeability of the fracture. For a linear joint, the shear displacement  $U_s$  can be calculated as:

$$U_s = \frac{\Delta\tau_n}{K_s} \quad (12)$$

where  $\Delta\tau_n$  is the excess shear stress deriving shear slippage, and it can be calculated as the difference between shear stress and shear strength:

$$\Delta\tau_n = \tau_n - \sigma_{eff} \tan(\varphi_{basic} + \varphi_{dil}^{eff}) \quad (13)$$

When the effective normal stress on fracture face becomes negative (e.g., when, the local pore pressure is higher than the in-situ stress), the fracture faces are no longer in contact. In this case, equation (12) reduces to (14) as:

$$U_s = \frac{\tau_n}{K_s} \quad (14)$$

The change in fracture aperture due to accumulated shear dilation in a time step can be expressed as:

$$a_s = U_s \tan(\varphi_{dil}^{eff}) \quad (15)$$

The total aperture after the shear can be obtained as ((Willis-Richards et al. 1996):

$$a = \frac{a_0}{1 + 9\sigma_{eff}/\sigma_{nref}} + a_s = \frac{a_0 + U_s \tan(\varphi_{dil})}{1 + \frac{9\sigma_{eff}}{\sigma_{nref}}} \quad (16)$$

The fracture apertures are updated at every time step as the stress state changes. Then the stress dependable permeability is calculated at every time step using the updated fracture apertures.

## **HEAT CONVECTION AND CONDUCTION**

In heat transfer calculations, the water flow through the rock matrix is ignored, therefore, the heat convection is confined within the interconnect fracture network. Heat exchange along the fracture face is estimated by assuming the heat conduction is perpendicular to the fracture face. Assuming that no energy is retained by the fluid stored within the fracture, the energy conservation is obtained at each fracture center by balancing the heat convection (from fluid flow) and heat conduction between adjacent rock mass and the fluid in the fracture. It is

assumed the temperature at fracture face is continuative (Brue 2002):

$$T_f = T_m \text{ at } y=0 \quad (17)$$

The energy balance equation can be expressed as:

$$dE_i = \sum_{out} \rho_f C_f q_{ij} T_{fj(t+\Delta t)} dt - \sum_{in} \rho_f C_f q_{ik} T_{fi(t)} dt \quad (18)$$

$q_{ij}$  and  $q_{ik}$  represents the fluxes flow in a given fracture  $i$ , from fracture  $j$  and flow out to fracture  $k$  with temperature  $T_{fj}$  and  $T_{fi}$ , respectively. Flow leaves with the same temperature as current temperature in fracture  $i$ .  $dE_i$  denotes the energy from the heat flux at fracture walls, which is governed by conduction (diffusive equation (19)). The shape of heat source rock block is assumed to be cylindrical with a radius equal to the fracture radius. The length of the cylinder is chosen so that the temperature on the other end of the cylinder remains unchanged. The results shows that the temperature changes will not develop at a long distances within test time period. Therefore, the cylinder to cylinder interaction and the thermal stress effects are ignored at this stage. According to characteristic length definition (e.g., Marin, 2010), the cylinder length of a rock mass with heat diffusivity of  $1.15 \times 10^{-6} \text{ m}^2/\text{s}$  is an approximately 12 m. This length ensures the temperature on the opposite end of the matrix block is unchanged during one year of heat transfer.

The heat exchange across the fracture face can be described as following set of (Brue 2002):

$$\begin{aligned} dE_i &= \Phi_i S_i dt \\ \Phi_i &= K_m (dT_m / dy)_{y=0} \end{aligned} \quad (19)$$

$$\alpha \Delta T_m = \frac{\partial T_m}{\partial t}$$

The above diffusive equation is solved using finite difference method. Given the fracture temperature at time  $t$ , the solution will return the temperature distribution from the fracture face to the other end of the rock cylinder in the rock mass. After that the heat flux  $\Phi_i$  can be obtained hence the energy exchanged  $dE_i$ . At each fracture center, one energy balance equation is set up, and the set of equations id solved for  $T_{fi}$  at each time step. Parameters that appear in the above equations are  $\rho_f$  is the fluid density,  $C_f$  is the solid heat capacity,  $\alpha$  is the heat diffusivity of rock mass,  $S_i$  is the fracture face area, and  $K_m$  is the heat conductivity of rock mass.

## **Conductive flow network**

In heat transfer part, the flow is confined within the connected fracture networks. Therefore, it is necessary to find out the connected fractures. Search

algorithms are used to determine the connectivity. Every fracture is checked for whether or not it belongs to a connected flow path. Then, dead ends and isolated fractures are removed. An iterative analysis is employed to do the searching.

We assume that the fluid flow pattern within fracture channels similar to the fluid flow pattern between approximately parallel surfaces. The modified cubic, giving the volumetric flux ( $\text{m}^3/\text{s}$ ) through a fracture with aperture  $a$  and length  $l$  is:

$$Q = \frac{-a^3 l}{12\mu} \frac{dp}{dl} \quad (20)$$

The flow network considers each connected fracture as a 1D pipe linking the centers of adjacent fractures (Fig. 5). Let  $k_i$  and  $k_j$  represent the conductivity of fracture  $i$  and  $j$ , and let  $p_i$  and  $p_j$  be the pore pressure at each fracture center.  $L_i$  and  $L_j$  are the channel length in fracture  $i$  and  $j$  respectively. The volumetric flow rate between fractures  $i$  and  $j$  can be write as (Brue et al. 1994):

$$Q_{ij} = k_{ij} \frac{p_i - p_j}{L_i + L_j} \quad k_{ij} = \frac{L_i + L_j}{L_i / k_i + L_j / k_j} \quad (21)$$

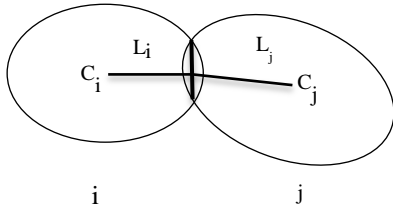


Figure 5: Flow channel between two connected fractures.  $C_i$  and  $C_j$  are centers of fractures  $i$  and  $j$ ,  $L_i$  and  $L_j$  are the channel lengths in fractures  $i$  and  $j$ , respectively.

Conductivity of each fracture can be obtained from the modified cubic law:

$$k_i = \frac{-a_i^3 L_i}{12\mu} \quad (22)$$

Generally, within the connect flow network, the flow mass conservation can be written at each fracture center as:

$$\sum_i Q_{ij} + source = 0 \quad (23)$$

Defining the boundary conditions and solving for the above set of equations, we can obtain  $Q_{ij}$  between

fractures  $i$  and  $j$ , which is used in the heat transfer calculation discussed above.

### NEAR WELLBORE REACTION SIMULATION

In order to investigate the near wellbore reaction, a small scale reservoir model of size  $40\text{m} \times 40\text{m} \times 20\text{m}$  is considered. Fig. 6 shows a half of the domain with the finite element mesh, and Fig. 7 shows the fractured zone that contains 500 stochastic fractures. Parameters used in this case are listed in Table 2. Rock properties are from experiment conducted on Newberry tuff core plugs (Li et al, 2012). A constant wellbore pressure increment is applied to this model. The outer boundary of the reservoir block is assumed to be a no flow boundary (Fig. 6).

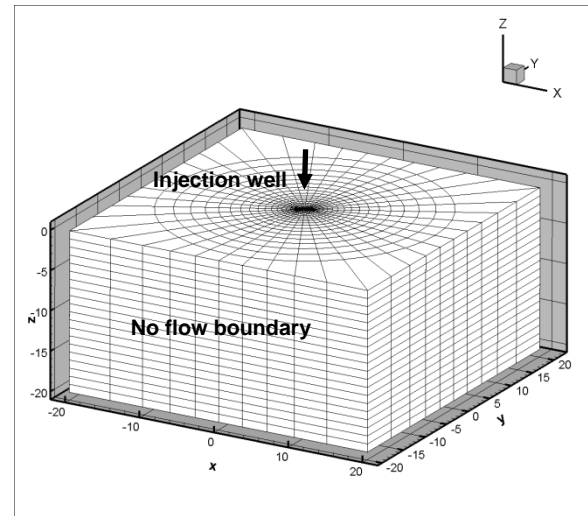


Figure 6: Finite element mesh of a small scale reservoir model.

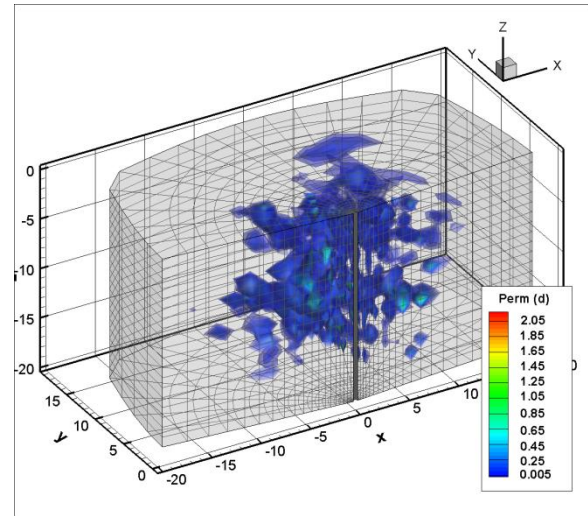


Figure 7: Fractured zone model with 500 stochastic fractures. Color bar shows the equivalent permeability of the fractured zone.

Table 2: Parameters used in near wellbore simulation.

<b>Rock properties</b>	
Model size (m <sup>3</sup> )	40 X 40 X 20
Young's modulus(GPa)	27.24
Poisson's ratio	0.4
Skempton's coefficient	1
Matrix permeability (md)	5
Porosity	0.025
Fluid density (kg/m <sup>3</sup> )	1000
Fluid bulk modulus (MPa)	3291
Fluid viscosity (Pa s)	1.0x10 <sup>-4</sup>
Fluid viscosity (Pa s)	1.0x10 <sup>-4</sup>
Fracture basic friction angle(degree)	50.2
Shear dilation angle(degree)	3.0
90% closure stress (MPa)	100
<b>Fracture properties</b>	
Fracture density(m <sup>-1</sup> )	1
Fisher parameter, $\kappa$	2.8
Mean fracture radial (lognormal)	0
Standard deviation of fracture radial, $s$	0.7
<b>Stress State</b>	
Vertical stress (MPa)	67
Maximum horizontal stress (MPa)	62
Minimum horizontal stress (MPa)	41
In-situ pore pressure (MPa)	25
Injection pressure (MPa)	5

Pore pressure developments after 2 hours of injection and the corresponding micro-seismic events are plotted in Fig. 8 and Fig. 9, respectively. Fig. 8 shows pore pressure distribution of three fracture networks with different stochastic parameters. In these figures,  $\kappa$  is the fracture orientation parameter and  $s$  is the fracture size parameter (Table 2). We can see from both the pore pressure and the seismic clouds that the fracture properties dramatically influence the stimulation results. The seismic events of the fracture network with Fisher von Mises orientation distribution are limited near the injection well. The randomly distributed fracture network has a larger zone of micro-seismic events and higher pore pressure build up. The fracture size also has influence on the permeability improvement result (Fig. 9 b and c). The location of shear slippage is different from each case. This phenomenon indicates the important role of characterizing fracture properties for reservoir stimulation modeling and design.

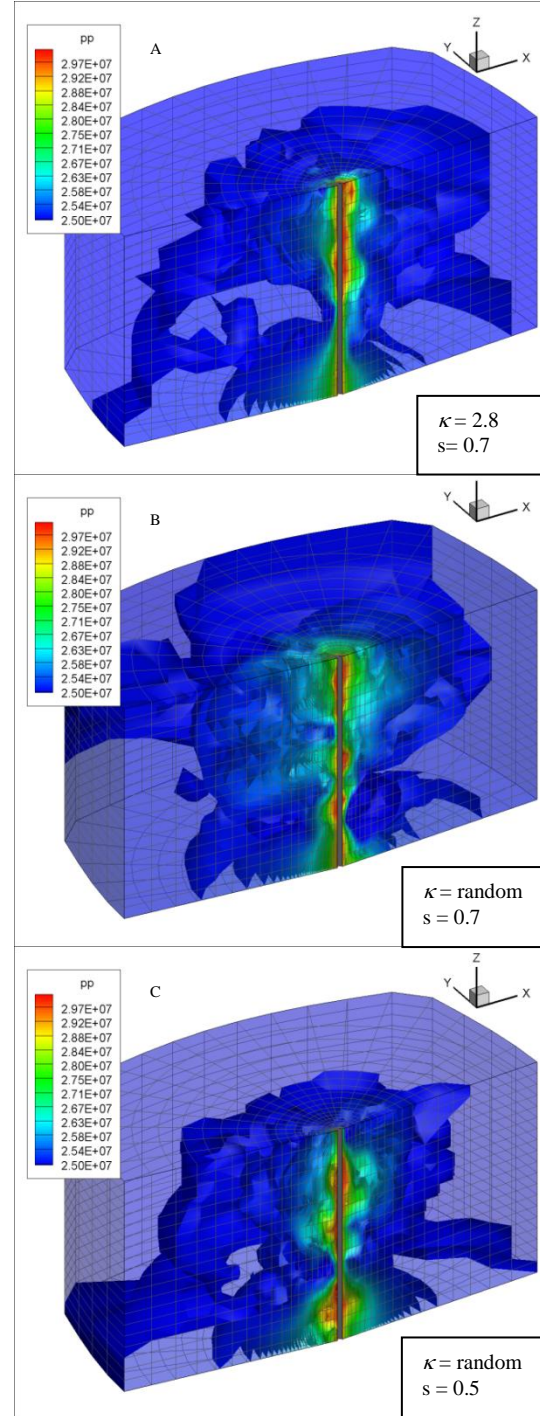


Figure 8: Pore pressure development at  $t = 2$  hour with fracture networks.

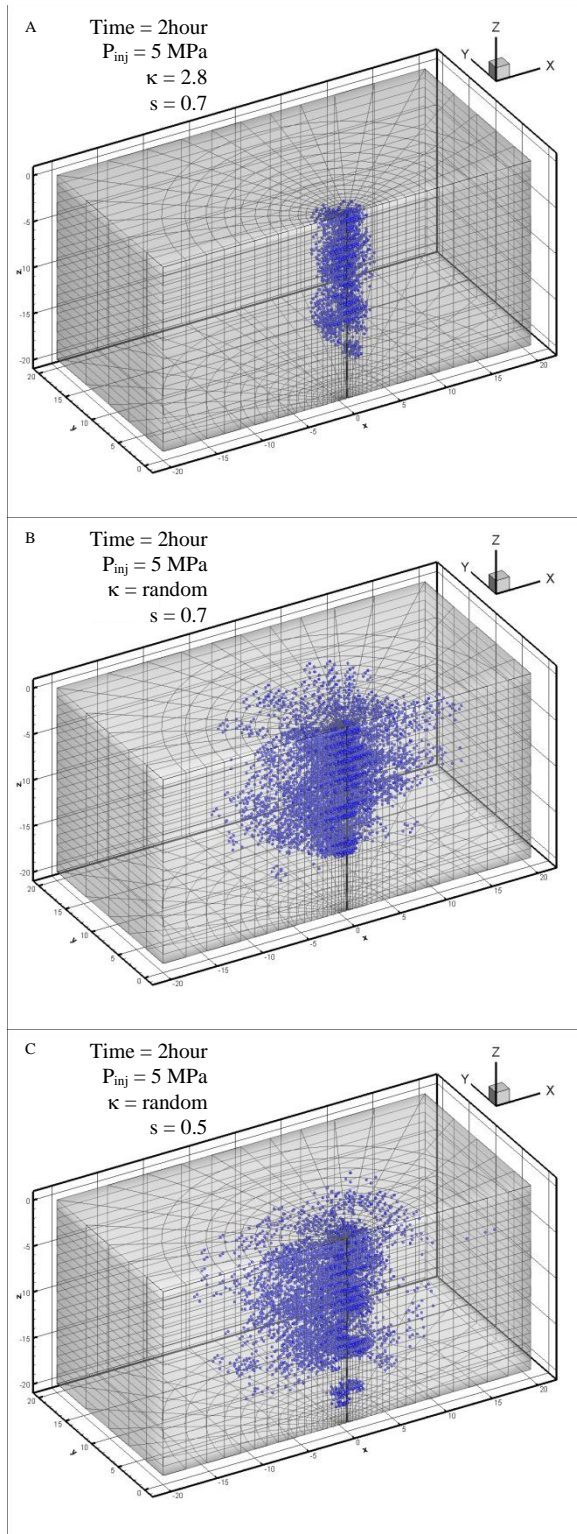


Figure 9: Micro-seismic events at  $t = 2$  hour of three blocks with different fracture properties.

To illustrate the permeability improvement, Fig. 10 shows the comparison of injection in two reservoirs have the same fracture networks, but with different

rock type. One of them (group B) is assumed to have rigid rock which does not allow failure during the injection. The other one (group A) has the same rock type as tested before. We can see that before shear dilation happens, the pore pressure distributions are the same in both reservoirs. After shear dilation, the pore pressure distribution in rock A is affected by the updated permeability, and higher pore pressure is shown in the upper zone (Fig. 10 A2). We can see from Fig. 10 A3 and B3, after 10 hours of injection, the pore pressure built-up in reservoir A has been delayed. Higher reservoir pressure is shown in Fig. 10 B3. This observation is resulted from the fracture opening and permeability increasing in reservoir A.

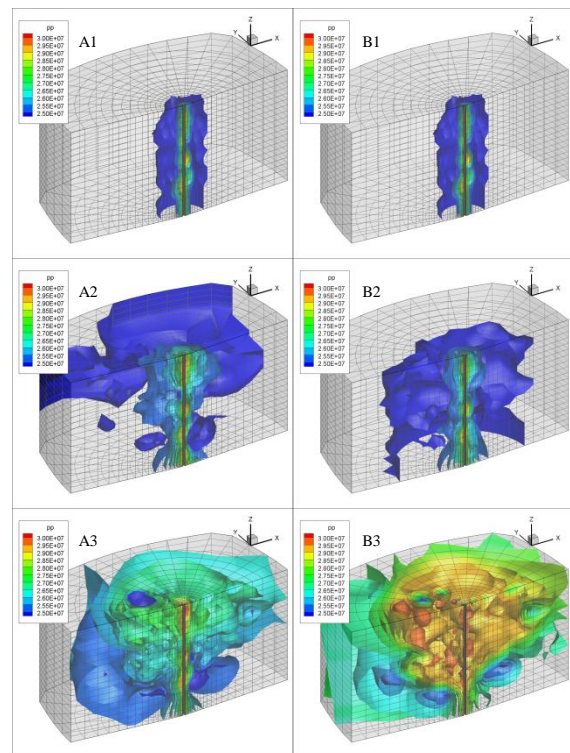


Figure 10: Iso-surfaces of pore pressure for reservoirs with (A) and without (B) permeability improvement.

The flow rate vs. time profile of the above two reservoirs is shown in Fig. 11. The green line shows the flow rate profile of a permeability improved reservoir. Red line shows the flow rate profile of rigid rock reservoir. We can see that, in the stimulated reservoir, the flow rate increases quickly after the shear dilation. Fig. 12 shows the seismic events at  $t = 5$  hour, when a large increase of flow rate is observed in Fig. 11. Large shear slippages are recorded, which is one of the reasons for the large increase of flow rate at  $t = 5$  hour. The flow rate will also increase when the injection fluid front reaches the higher permeability zones. Therefore, we can see periodic increase of flow rate from both curves. To

show the permeability improvement, slices of permeability contours of the reservoir A at  $t = 4$  hour and  $t = 5$  hour are plotted in Fig 13. Permeability changes at all locations of shear slippage shown in Fig. 12. But, all the change cannot be shown in a single contour map because of the rather broad range of permeability values ( $5 \times 10^{-16} \text{ m}^2$  to  $6.2 \times 10^{-8} \text{ m}^2$ ) within the simulation domain. Therefore, only the values in the range of  $2.5 \times 10^{-13} \text{ m}^2$  to  $8.5 \times 10^{-11} \text{ m}^2$  are potted in Fig. 13. The results show the correlations between seismic events, permeability improvement, and flow rate increase.

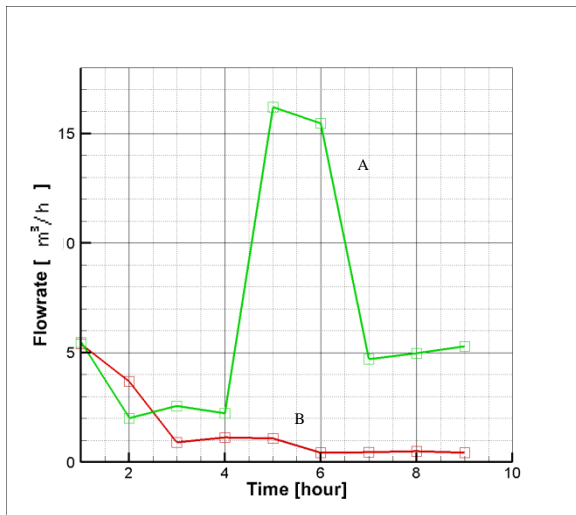


Figure 11: wellbore flow rate profile with time for reservoirs with (A) and without (B) permeability improvement.

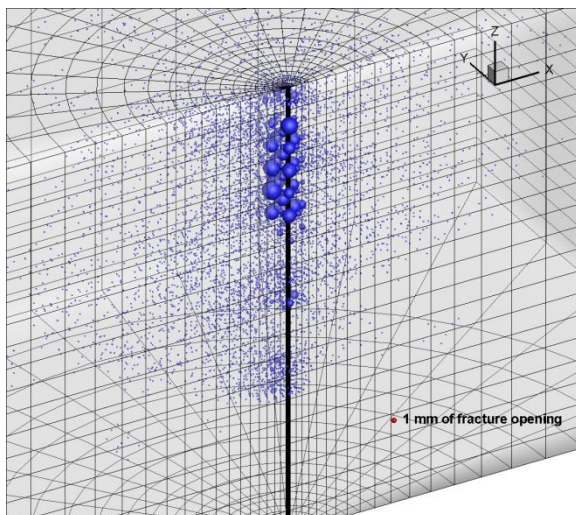


Figure 12: Micro-seismic events plot at  $t = 5$  hours. Bubble size indicates the shear slippage value.

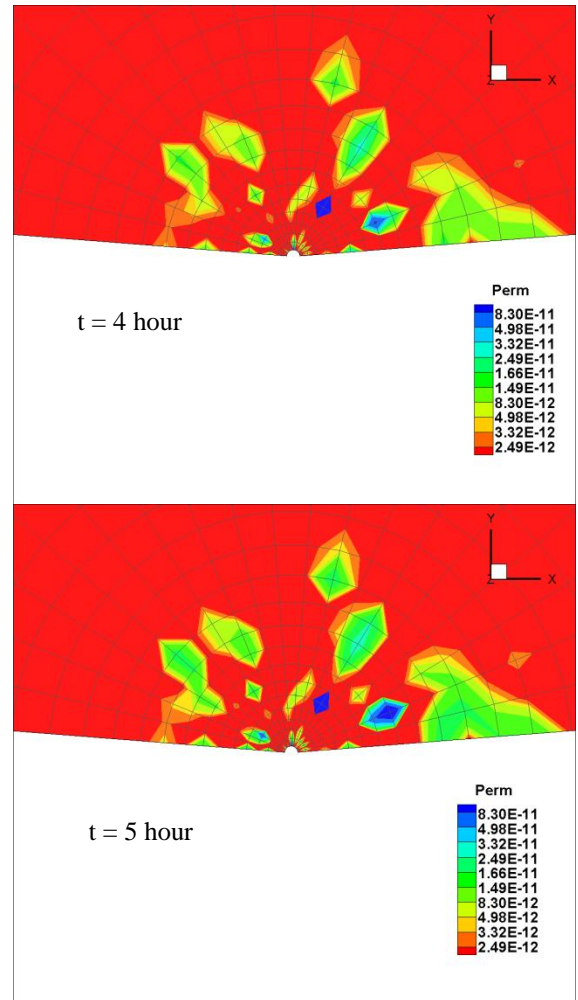


Figure 13: Near well permeability showing the center layer at  $t = 4$  hours and  $t = 5$  hours. Only 25 Darcy to 850 Darcy permeability range is plotted for the best illustration.

### HEAT TRANSFER WITHIN CONNECTED FRACTURES

Heat transfer simulation in this work is assumed to be independent from the poroelastic process. Only the resulting fracture geometry from poroelastic process is considered to vary with time during heat transfer calculations.

To illustrate the temperature distribution within the flow path, a segment of the flow path is cut out and is shown in Fig. 14 in a 2D view. It is a three dimension network of one dimensional flow pipes. Heat conductivity of each pipe is depending on the fracture apertures and the distance between two adjacent fractures. The heat convection from adjacent rock body is depending on the flow rate and temperature within the fractures. In this test example, it is assumed the injection fluid temperature is  $10 \text{ }^\circ\text{C}$  and

the reservoir temperature is 300 °C. the flowing time is 10 minutes.

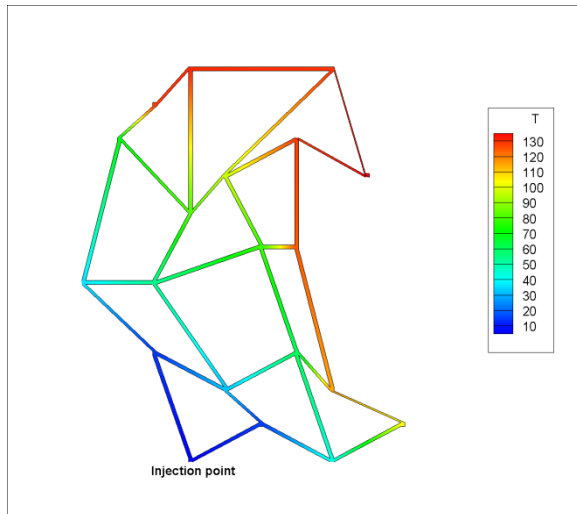


Figure 14: A heat transfer example of a flow path consisting of 20 fractures.

## CONCLUSIONS

A three-dimensional poroelastic FEM model with stochastic fracture network has been developed to simulate permeability enhancement in EGS. The model is capable of analyzing the stress variations, pore pressure distributions, induced micro-seismicity, and heat transfer during injection. Heat transfer is decoupled from poroelastic analysis. Results from example simulations show the important role of fracture network properties (fracture distribution, orientation, and fracture network connectivity) in geothermal reservoir design and development. The fracture aperture changes with stress variations associated with injection and directly influence the reservoir permeability evolution. The orientation of the fractures in the reservoir dogmatically influences the permeability development. In a fractured reservoir, properties of fracture network have a significant impact on pore pressure and seismic events distribution. The permeability change also affects the heat transfer with in the fractures. Test examples were also used to simulate the potential for induced seismicity. Results show a correlation between pore pressure increase, fracture slip and MEQs. A comparison with field/lab test needs to be conducted in the future work. Calibration of fracture distribution parameters and damage induced permeability change are being considered and will be reported in the future.

## REFERENCES

Brue.D. (2002), "Impact of Induced Thermal Stresses During Circulation Tests in An Engineered Fractured Geothermal Reservoir; Example of

The Soultz-sous-Forets European Hot Fractured Rock Geothermal Project, Rhine Graben, France," *Oil and Gas Scienceand Technology Rev IFP*, **57** , 459–470.

Brue, D.,Cacas, M.C., Ledoux,E, and Marsily, G. (1994), "Modelling Storage Behaviour in a Fractured Rock Mass," *Journal of Hydrology*, **162**, 267-278.

Cacas, M. C., Ledoux, E., De Marsily, G. and Tillie, B. (1990), "Modeling Fracture Flow with A Stochastic Discrete Fracture Network: Calibration and Validation: 1. The Flow Model," *Water Resources Research*, **26(3)**, 479-489.

Cladouhos, T. Clyne, M., Nichols, M. Petty, S., Osborn, W. and Nofziger, L. 2011, "Newberry Volcano EGS demonstration stimulation Modeling," *GRC Transactions*, **35**, 2011.

Dershowitz, W. S. and Einstein, H. H. (1988), "Characterizing Rock Joint Geometry with Joint System Models," *Rock Mechanics and Rock Engineering*, **21**, 21-51.

Ghassemi, A., Tarasovs, S., and Cheng, A. H.-D. (2007), "A Three-Dimensional Study of The Effects of Thermo-Mechanical Loads on Fracture Slip in Enhanced Geothermal Reservoir," *International Journal for Rock Mechanics & Mining Science* **44**, 1132–1148.

Kolditz, O., and Clauser, C. (1998), "Numerical Simulation of Flow and Heat Transfer in Fractured Crystalline Rocks: Application to The Hot Dry Rock Site in Rosemanowes (U.K.)," *Geothermics*, **27**, 1-23.

Lee, S. H. and Ghassemi, A. (2011), "Three-dimensional Thermo-Poro-Mechanical Modeling of Reservoir Stimulation and Induced Micro-seismicity in Geothermal Reservoir," *Thirty-Sixth Workshop on Geothermal Reservoir Engineering, Stanford University, Stanford, California*.

Li, Y., Wong, J., and Ghassemi, A. (2011), "Mechanical Properties of Intact and Jointed Welded Tuff from Newberry Volcano," *Thirty-Seventh Workshop on Geothermal Reservoir Engineering, Stanford University (in press), Stanford, California*.

Marin, E. (2010), "Characteristic dimensions for heat transfer," *Latin American Journal of Physics Education*, **4**.

Rahman, M. K., Hossain, M. M. and Rahman, S. S. (2002), "a Shear-dilation-based Model for Evaluation of Hydraulically Stimulated Naturally

Fractured Reservoirs,” *Innational Journal for Numerical and Analytical Methods in Geomechanics.*, **26**,469-497.

Tezuka, K. and Watanabe, K. (2000), “Fracture Network Modeling of Hijiori Hot Dry Rock Reservoir by Deterministic and Stochastic Crack Network Simulator (D/SC),” *Proceeding World Geothermal Congress 2000*.

Tezuka, K., Tamagawa, T. and Watanabe, K. (2005), “Numerical Simulation of Hydraulic Shearing in Fracture Reservoir,” *Proceeding World Geothermal Congress 2005*.

Wang,X. and Ghassemi,A. (2011), “a Three-Dimensional Stochastic Fracture Network Model for Geothermal Reservoir Stimulation,” *Thirty-Sixth Workshop on Geothermal Reservoir Engineering (in press), Stanford University, Stanford, California*.

Willis-Richards, J., Watanabe, K. and Takahashi, H. (1996),”Progress Toward A Stochastic Rock Mechanics Model of Engineered Geothermal Systems,” *Journal of Geophysical Research*, **101**, 481-496.

Zhou,X. and Ghassemi, A. (2009) “Finite Element Analysis of Coupled Chemo-poro-thermo-mechanical Effects Around a Wellbore in Swelling Shale.” *International Journal of Rock Mechanics and Mining Science*, **46**,769-778.

Zimmerman, R. W. and Bodvarsson, G. S. (1996), “Hydraulic Conductivity of Rock Fractures,” *Transport in Porous Media*, **23**, 1-30.

ALTAROCK ENERGY INC. (2011) “Newberry Volcano EGS Demonstration Stimulation Planning,” *GRC Annual Meeting, October 25, 2011*.